Articles

Comprehensive Theoretical Study on the Mechanism of Regioselective Hydroformylation of Phosphinobutene Catalyzed by a Heterobinuclear Rhodium(I)−Chromium Complex

Dianyong Tang, Song Qin, Zhishan Su, and Changwei Hu*

Key Laboratory of Green Chemistry and Technology (Sichuan University), MOE, College of Chemistry, Sichuan University, Chengdu 610064, People's Republic of China

Received February 19, 2006

A concerted mechanism for the hydroformylation of phosphinobutene catalyzed by the heterobinuclear complex $(CO)_4Cr(\mu\text{-}PH_2)_2RhH(CO)(PH_3)$ was elucidated by density functional theory (DFT), with particular emphasis on the catalytic cycle, the regioselectivity, the cooperativity of Cr with Rh, and the interpretation of experimental observations. Four possible mechanisms were investigated, and the results were compared. It is found that the introduction of the $Cr(CO)_4$ moiety remodels the mechanism. The Rh−Cr-catalzyed hydroformylation mechanism includes the following: (a) formation of the chelate acyl species through a chelate associative mechanism including olefin addition, olefin insertion, and carbonyl insertion steps, (b) CO addition to the chelate acyl species with the formation of a monodentate acyl species, and (c) the conversion of the monodentate acyl species to the product aldehyde through H_2 coordination, H_2 oxidative addition, and aldehyde elimination. Carbonyl insertion is predicted to be the rate-limiting step, with a free energy barrier of 86.76 kJ/mol in benzene solution at 353.15 K and 27.15 atm. The favorability of the branched product is predicted to be nearly 100% both kinetically and thermodynamically. The chromium serves as an orbital reservoir in olefin addition and insertion steps via the variation of the orbital interaction between Rh and Cr atoms. The catalytic activity of the Rh(I)−Cr bimetallic complex is higher than that of the monometallic Rh catalysts. These could explain satisfactorily the reported experimental observations.

Introduction

Hydroformylation is one of the largest industrial homogeneous catalytic processes in the world, producing more than 6,000,000 tons of aldehydes each year.[1] In this process, alkenes react with hydrogen and carbon monoxide to give either linear or branched aldehydes (Scheme 1; R = alkyl).

The most popular hydroformylation catalysts employed in industry are low-valent Co and Rh complexes, although a number of other catalysts based on Pt, Ru, Ir, and Pd have been utilized in asymmetric hydroformylation.[2,3] The use of heterobimetallic complexes as catalysts in the hydroformylation reaction is of interest with regard to the possibilities of using the adjacent metal center to increase the catalytic activity and selectivity.[4−11] The heterobimetallic catalysts $(CO)_4M(\mu\text{-}PPh_2)_2RhH(CO)(PPh_3)$ (M = Cr, Mo, W) (Chart 1) can achieve 100% branched product and 100% conversion of olefin for the hydroformylation.[4−6] Rida et al. employed the heterobimetallic complex $[(\eta^5\text{-}C_5H_5)Ru(\mu\text{-}CO)_2(\mu\text{-}\eta^2\text{-}HC(PPh_2)_3RhCl_2)$ as catalyst for the hydroformylation of 1-octene, and 89.9% linear product at 40% conversion was achieved; the monometallic Rh catalyst could only give 50% linear product under the same reaction conditions.[7]

Scheme 1

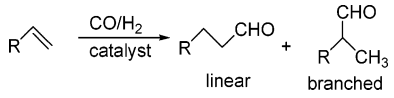

The widely accepted mechanism for olefin hydroformylation employing the catalyst $HRh(PR_3)_3(CO)$ was originally proposed in 1970 by Wilkinson et al., and two possible mechanisms were

* To whom correspondence should be addressed. E-mail: gchem@scu.edu.cn or chwehu@mail.sc.cninfo.net. Fax/tel: +86-28-85411105.

(1) Frohning, C. D.; Kohlpaintner, C. W. Hydroformylation (oxo synthesis, Roelen reaction). In *Applied Homogeneous Catalysis with Organometallic Compounds*; Cornils, B., Herrmann, W. A., Eds.; VCH: New York, 1996; Vol. 1.

(2) Agbossou, F.; Carpentier, J. F.; Mortreux, A. *Chem. Rev.* **1995**, *95*, 2485−2506.

(3) Breit, B.; Seiche, W. *Synthesis* **2001**, 1−36.

(4) Dickson, R. S.; Simone, T. D.; Campi, E. M.; Jackson, W. R. *Inorg. Chim. Acta* **1994**, *220*, 187−192.

(5) Coutinho, K. J.; Dickson, R. S.; Fallon, G. D.; Jackson, W. R. Simone, T. D.; Skelton, B. W.; White, A. H. *J. Chem. Soc., Dalton Trans.* **1997**, 3193−3199.

(6) Dickson, R. S.; Bowen, J.; Campi, E. M.; Jackson, W. R.; Jonasson, C. A. M.; McGrath, F. J.; Paslow, D. J.; Polas, A.; Renton, P.; Gladiali, S. *J. Mol. Catal. A: Chem.* **1999**, *150*, 133−146.

(7) Rida, M. A.; Smith, A. K. *J. Mol. Catal. A: Chem.* **2003**, *202*, 87−95.

(8) Baricelli, P. J.; López-Linares, F.; Bruss, A.; Santos, R.; Lujano, E.; Sánchez-Delgado, R. A. *J. Mol. Catal. A: Chem.* **2005**, *239*, 130−137.

(9) Ungváry, F. *Coord. Chem. Rev.* **2005**, *249*, 2946−2961.

(10) Gladiali, S.; Pinna, L.; Arena, C. G.; Rotondo, E.; Faraone, F. *J. Mol. Catal.* **1991**, *66*, 183−190.

(11) Broussard, M. E.; Juma, B.; Train, S. G.; Peng, W.-J.; Laneman, S. A.; Stanely, G. G. *Science* **1993**, *260*,1784−1788.

10.1021/om0601605 CCC: $37.00
Publication on Web 12/08/2006

Chart 1. The Rh−Cr Heterobimetallic Catalyst

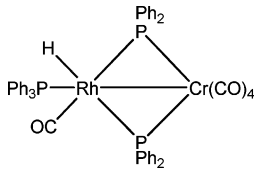

Scheme 2. Catalytic Cycle Proposed by Coutinho et al.[5]

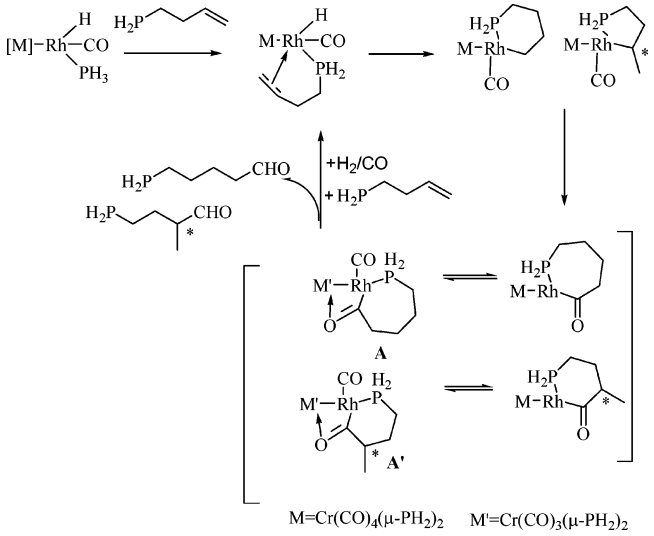

suggested: a dissociative mechanism with seven elementary steps, including catalyst generation, olefin addition, olefin insertion, carbonyl addition, carbonyl insertion, H_2 oxidative addition, and aldehyde elimination (Scheme S1, Supporting Information), and an associative mechanism composed of olefin addition, olefin insertion, carbonyl insertion, H_2 oxidative addition, and aldehyde elimination (Scheme S2, Supporting Information).[12−14] The associative mechanism was proved to be unfavorable because it involves a 20-electron olefin intermediate. Experimental evidence suggests that H_2 oxidative addition should be the rate-limiting step. With reference to Wilkinson's catalytic cycle, Coutinho et al. proposed a catalytic cycle of hydroformylation catalyzed by Rh−M (M = Cr, Mo, W) heterobimetallic complexes, which is displayed in Scheme 2.[5] Their mechanistic studies demonstrated that the conversion of the acyl complexes **A** and **A′** into phosphinoaldehyde complexes must involve CO as well as H_2 (Scheme 2). Their results also clarified that this conversion required a slow, reversible oxidative addition of hydrogen to the acyl compound forming the dihydride species, which only produces the coordinated aldehyde complexes in the presence of CO.[5,6]

Thanks to enormous progress in methods of computational chemistry in the field of transition-metal-catalyzed reactions,[15] since 1997, many theoretical studies on hydroformylation have been published, some of which also deal with issues of regioselectivity or stereoselectivity.[16−24] Schmid et al. treated some hydroformylation preequilibria with the model ligands PH_3 and PMe_3 using ab initio and DFT methods.[25] The first calculation of the whole catalytic cycle (ligand PH_3, substrate ethene) at the ab initio level was reported by Morokuma et al.[26] Calculations with the hybrid density functional B3LYP were reported for systems containing PH_3,[27,28] monophosphane ligands with various alkyl and phenyl substitutions,[29] and even a bis-phosphane chelate of real size.[30−32] Recently, Gleich et al.[33] employed static (Gaussian)[34] and dynamic (CPMD) BP86 methods to study unmodified and three modified (PH_3, PF_3, and PMe_3) Rh-based catalysts for the hydroformylation of ethene.

So far, only the catalytic cycles of hydroformylation catalyzed by monometallic Rh or Co catalysts had been investigated by means of quantum-mechanical methods. On the basis of the catalytic cycle proposed by Coutinho et al. (Scheme 2), the present theoretical mechanistic investigation on the modeled catalyst $(CO)_4Cr(\mu\text{-}PH_2)_2RhH(CO)(PH_3)$ is aimed at extending the understanding of the hydroformylation of alkenes catalyzed by the Rh−Cr heterobimetallic complex by elucidating the following intriguing, but not yet firmly resolved, aspects:

(1) Which is the preferred mechanism for the hydroformylation reaction of phosphinobutene catalyzed by the Rh−Cr heterobimetallic complex: the associative or dissociative mechanism?

(2) Where does the regioselectivity originate from?

(3) How does the cooperative chromium affect the activity of the catalyst and the regioselectivity of the reaction?

(4) Which conformations of the metallacycle are preferred in the catalytic cycle?

The present computational study is, to the best of our knowledge, the first detailed comprehensive theoretical mechanistic investigation of the complete reaction cycle for the hydroformylation catalyzed by a heterobimetallic $(CO)_4Cr(\mu\text{-}PH_2)_2RhH(CO)(PH_3)$ complex.

Models and Computational Details

The present computations were based on the hydroformylation reaction of phosphinobutene ($CH_2{=}CHCH_2CH_2PPh_2$) catalyzed by

(12) Evans, D.; Yagupsky, G.; Wilkinson, G. *J. Chem. Soc. A* **1968**, 2660−2665.
(13) Evans, D.; Yagupsky, G.; Wilkinson, G. *J. Chem. Soc. A* **1968**, 2665−2671.
(14) Evans, D.; Osborn, J. A.; Wilkinson, G. *J. Chem. Soc. A* **1968**, 3133−3142.
(15) Torrent, M.; Sola, M.; Frenking, G. *Chem. Rev.* **2000**, *100*, 439−493.
(16) Gleich, D.; Schmid, R.; Herrmann, W. A. *Organometallics* **1998**, *17*, 4828−4834.
(17) Rocha, W. R.; de Almeida, W. B. *Int. J. Quantum Chem.* **2000**, *78*, 42−51.
(18) Carbó, J. J.; Maseras, F.; Bo, C.; van Leeuwen, P. W. N. M. *J. Am. Chem. Soc.* **2001**, *123*, 7630−7637.
(19) Decker, S. A.; Cundari, T. A. *J. Organomet. Chem.* **2001**, *635*, 132−141.
(20) Alagona, G.; Ghio, C.; Lazzaroni, R.; Settambolo, R. *Organometallics* **2001**, *20*, 5394−5404.
(21) Gleich, D.; Schmid, R.; Herrmann, W. A. *Organometallics* **1998**, *17*, 2141−2143.
(22) Gleich, D.; Herrmann, W. A. *Organometallics* **1999**, *18*, 4354−4361.
(23) Paciello, R.; Siggel, L.; Röper, M. *Angew. Chem.* **1999**, *111*, 2045−2048; *Angew. Chem., Int. Ed.* **1999**, *38*, 1920−1921.
(24) Paciello, R.; Siggel, L.; Kneuper, H.-J.; Walker, N.; Röper, M. *J. Mol. Catal. A: Chem.* **1999**, *143*, 85−97.
(25) Schmid, R.; Herrmann, W. A.; Frenking, G. *Organometallics* **1997**, *16*, 701−708.
(26) Matsubara, T.; Koga, N.; Ding, Y.; Musaev, D. G.; Morokuma, K. *Organometallics* **1997**, *16*, 1065−1078.
(27) Gleich, D. In *Applied Homogeneous Catalysis with Organometallic Compounds*; Cornils, B., Herrmann, W. A., Eds.; Wiley-VCH: Weinheim, Germany, 2002; Vol. 2, pp 727−737.
(28) Decker, S. A.; Cundari, T. R. *Organometallics* **2001**, *20*, 2827−2841.
(29) Decker, S. A.; Cundari, T. R. *New J. Chem.* **2002**, *26*, 129−135.
(30) Landis, C. R.; Uddin, J. *Dalton Trans.* **2002**, 729−742.
(31) Svensson, M.; Humbel, S.; Fröse, R. D. J.; Matsubara, T.; Sieber, S.; Morokuma, K. *J. Phys. Chem.* **1996**, *100*, 19357−19363.
(32) Bakowies, D.; Thiel, W. *J. Phys. Chem.* **1996**, *100*, 10580−10594.
(33) Gleich, D.; Hutter, J. *Chem. Eur. J.* **2004**, *10*, 2435−2444.
(34) Frisch, M. J.; Trucks, G. W.; Schlegel, H. B.; Scuseria, G. E.; Robb, M. A.; Cheeseman, J. R.; et al. *Gaussian 03*, Revision B.05; Gaussian, Inc., Pittsburgh, PA, 2003.

Scheme 3. Computational Models ($R_1 = CH_2CH_2PH_2$)

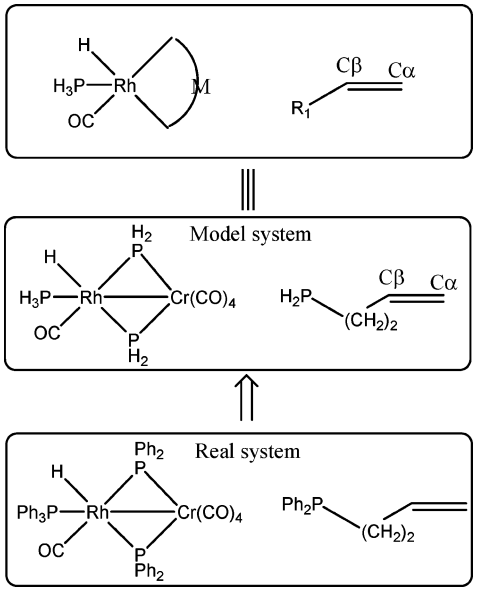

the Rh(I)−Cr complex $(CO)_4Cr(\mu\text{-}PPh_2)_2RhH(CO)(PPh_3)$.[5] $(CO)_4Cr(\mu\text{-}PH_2)_2RhH(CO)(PH_3)$ and $CH_2{=}CHCH_2CH_2PH_2$ were chosen to mimic the catalyst and the reactant, respectively, to minimize the computational time (Scheme 3).

All computations were performed by using Gaussian03 package.[34] Geometries for all the intermediates and the transition states were optimized by means of the density functional theory (DFT) with Becke's three-parameter functional (B3)[35] plus Lee, Yang, and Parr (LYP)[36,37] correlation functional. The double-ζ quality Hay and Wadt LANL2DZ[38−40] basis sets for the valence and penultimate shells with effective core potentials for Rh, Cr, Mo, and P were used, and a set of f polarization functions with an exponent of 1.35[41] for Rh and a set of d polarization functions with an exponent of 0.371[42] for P were added. For other atoms, the 6-31G(d,p) [43−52] basis sets were utilized. This basis set was referred to as **631LANp**. In addition, we also carried out the test calculations on the μ-acyl complex **A′**(Mo) to check if our computational model and level were able to reproduce the experimentally reported structural parameters. As shown in Figure 1, the structure of the μ-acyl complex **A′**(Mo) calculated at the B3LYP/**631LANp** level is very close to that determined by X-ray crystallography.[5]

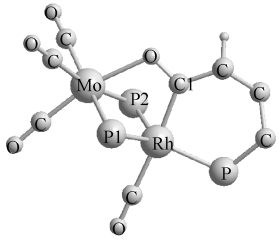

Rh-Mo	2.85(2.78)
Rh-P1	2.40(2.32)
Rh-P2	2.41(2.34)
Rh-C1	2.06(2.05)
Rh-P	2.34(2.29)
Mo-P1	2.52(2.47)
Mo-P2	2.51(2.49)
Mo-O	2.32(2.25)
Rh-Mo-P1	52.8(52.1)
Rh-Mo-P2	52.8(52.4)
Rh-Mo-O	65.0(66.4)
P1-Mo-P2	105.3(103.9)
P1-Mo-O	78.5(78.7)
Rh-Mo-C1	72.2(71.9)

Figure 1. Optimized parameters for the μ-acyl complex **A′**(Mo) at the B3LYP/**631LANp** level and those obtained by X-ray crystallography (in parentheses).

Transition-state structures were located until the Hessian matrix had only one negative value, and the transition states were also verified by animating the eigenvectors' coordinates of the sole imaginary frequency with a visualization program (Molden).[53] Zero-point energies and thermal corrections had also been computed in the rigid rotator−harmonic oscillator approximation to obtain the free energies under the experimental conditions (353.15 K, 27.22 atm).[5] Natural charges were calculated by the natural population analysis at the same level as that used for geometry optimization.[54] With regard to the entropy effects, the following discussions were based on the free energies (ΔG) of activation and reaction. To evaluate the solvent effects, the self-consistent reaction field (SCRF) single-point energy calculations on the gas-phase-optimized structures in the benzene continuum (benzene as solvent) were carried out by using Tomasi's polarized continuum model (IEF-PCM)[55] with the UAHF topological model at the same level as that used for geometry optimization. The solvation free energy is the difference of the free energies in solution and the gas phase.

Results and Discussion

1. Structure of the Catalyst. The optimized structures of **1** are shown in Figure 2. The optimized stable structures of the catalyst $[(CO)_4Cr(\mu\text{-}PH_2)_2RhH(CO)(PH_3)]$ adopt the trigonal-bipyramidal configuration for the rhodium coordinate center. As shown in Figure 2, there are two possible isomers for the catalyst: one with the hydride trans to the PH_3 ligand (labeled **1a**) and the other with the hydride ligand trans to the CO ligand (labeled **1b**). The calculated structural and energetic data for **1a**,**b** are given in Figures 2 and 3.

The Rh−H bond in **1a** is shorter than that in **1b** by 0.03 Å. This difference should be attributed to the different trans influences of PH_3 and CO (CO > PH_3). The different Rh−Cr distances in **1a**,**b** should also result from the different trans influences of PH_3 and CO. As shown in Figure 3, catalyst **1a** is more stable than **1b**. The calculated vibrational frequencies of ν(Rh−H) are 2086 cm^{-1} for **1a** and 1992 cm^{-1} for **1b**, which is in agreement with the experimental result (2054 cm^{-1}).[5] The Rh−Cr distances (Figure 2), the Wiberg bond indices of Rh−Cr (0.19 and 0.20 au for **1a**,**b**), and the HOMO-3 orbitals of **1a**,**b** (Figure 2) indicate that the typical orbital interaction is between 4d of rhodium and 3d of chromium.

As shown in Figure 2, the rhodium center of species **1a**,**b** has five ligands, which is the same as for the precursor [HRh-

(35) Becke, A. D. *J. Chem. Phys.* **1993**, *98*, 5648−5652.
(36) Lee, C.; Yang, W.; Parr, R. G. *Phys. Rev. B* **1998**, *37*, 785−789.
(37) Miehlich, B.; Savin, A.; Stoll, H.; Preuss, H. *Chem. Phys. Lett.* **1989**, *157*, 200−205.
(38) Hay, P. J.; Wadt, W. R. *J. Chem. Phys.* **1985**, *82*, 270−283.
(39) Wadt, W. R.; Hay, P. J. *J. Chem. Phys.* **1985**, *82*, 284−299.
(40) Hay, P. J.; Wadt, W. R. *J. Chem. Phys.* **1985**, *82*, 299−310.
(41) Ehlers, A. W.; Dapprich, B. S.; Gobbi, A.; Hollwarth, A.; Jonas, V.; Kohler, K. F.; Stegmann, R.; Veldkamp, A.; Frenking, G. *Chem. Phys. Lett.* **1993**, *208*, 111−114.
(42) Check, C. E.; Faust, T. O.; Bailey, J. M.; Wright, B. J.; Gilbert, T. M.; Sunderlin, L. S. *J. Phys. Chem. A* **2001**, *105*, 8111−8116.
(43) Ditchfield, R.; Hehre, W. J.; Pople, J. A. *J. Chem. Phys.* **1971**, *54*, 724−728.
(44) Hehre, W. J.; Ditchfield, R.; Pople, J. A. *J. Chem. Phys.* **1972**, *56*, 2257−2261.
(45) Hariharan, P. C.; Pople, J. A. *Mol. Phys.* **1974**, *27*, 209−214.
(46) Gordon, M. S. *Chem. Phys. Lett.* **1980**, *76*, 163−168.
(47) Hariharan, P. C.; Pople, J. A. *Theor. Chim. Acta* **1973**, *28*, 213−222.
(48) Blaudeau, J.-P.; McGrath, M. P.; Curtiss, L. A.; Radom, L. *J. Chem. Phys.* **1997**, *107*, 5016−5021.
(49) Francl, M. M.; Pietro, W. J.; Hehre, W. J.; Binkley, J. S.; DeFrees, D. J.; Pople, J. A.; Gordon, M. S. *J. Chem. Phys.* **1982**, *77*, 3654−3655.
(50) Binning, R. C., Jr.; Curtiss, L. A. *J. Comput. Chem.* **1990**, *11*, 1206−1209.
(51) Rassolov, V. A.; Pople, J. A.; Ratner, M. A.; Windus, T. L. *J. Chem. Phys.* **1998**, *109*, 1223−1229.
(52) Rassolov, V. A.; Ratner, M. A.; Pople, J. A.; Redfern, P. C.; Curtiss, L. A. *J. Comput. Chem.* **2001**, *22*, 976−984.
(53) Schaftenaar, G.; Noordik, J. H. *J. Comput.-Aided Mol. Des.* **2000**, *14*, 123−134.
(54) Reed, A. E.; Weinstock, R. B.; Weinhold, F. *J. Chem. Phys.* **1985**, *83*, 735−746.
(55) Cossi, M.; Scalmani, G.; Rega, N.; Barone, V. *J. Chem. Phys.* **2002**, *117*, 43−54.

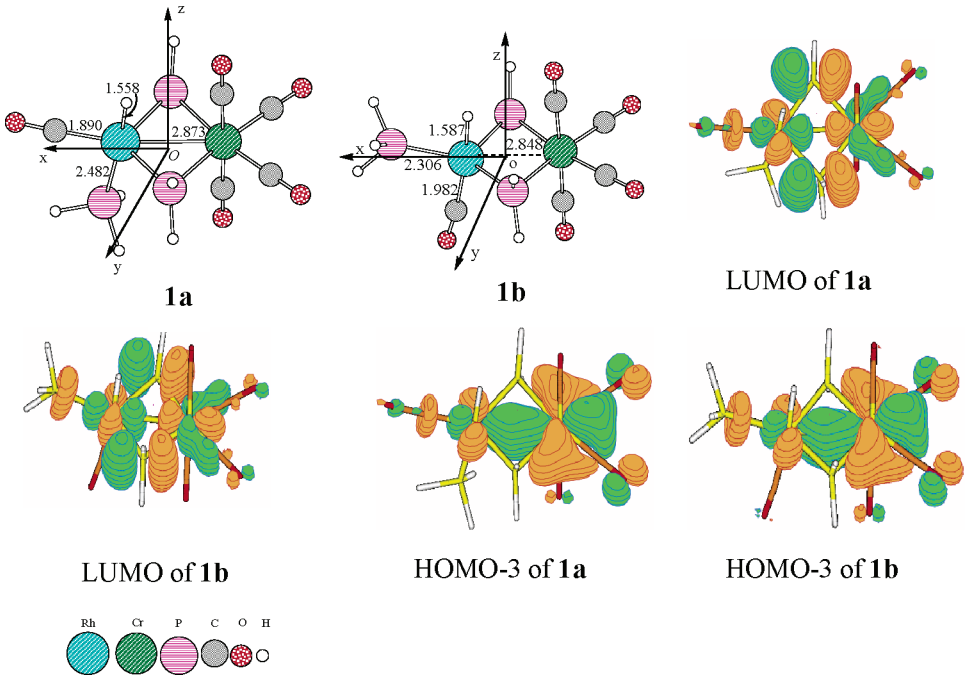

Figure 2. Optimized structures and LUMO and HOMO-3 molecular orbitals of catalysts **1a**,**b**. The bond lengths are given in angstroms.

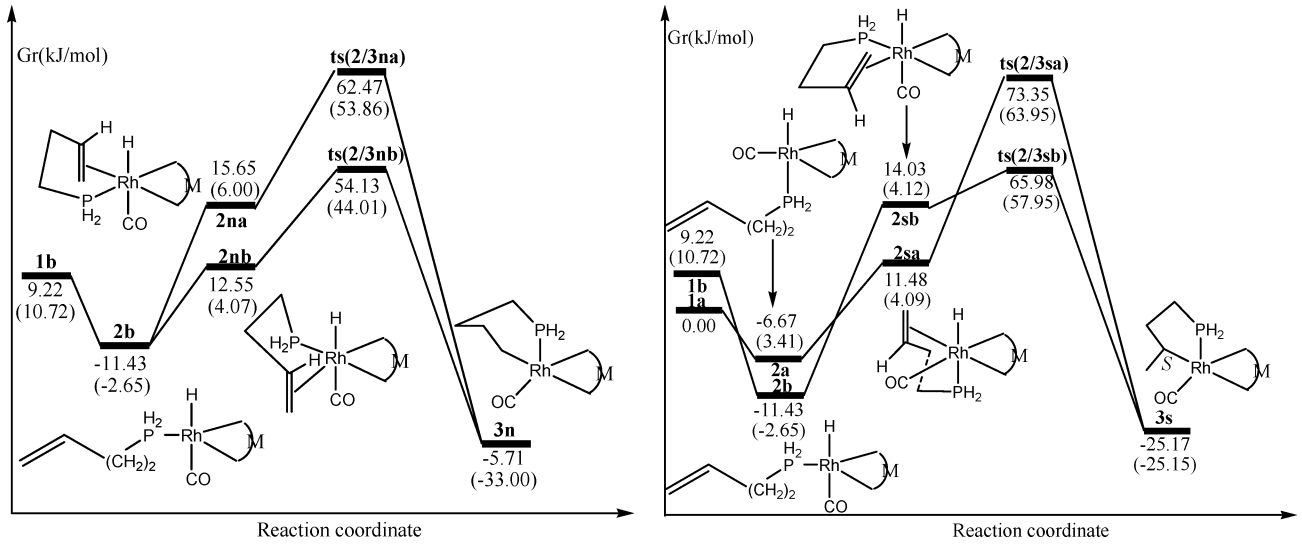

Figure 3. Free energy profiles of phosphinobutene addition and insertion steps of the chelate associative mechanism in the gas phase and benzene solution (values in parentheses) at 353.15 K and 27.22 atm.

$(PPh_3)_3(CO)$] of the monometallic catalyst [$HRh(PPh_3)_2(CO)$]. Could the bimetallic catalysts serve directly as the active catalyst? The olefin addition requires that the Rh center of the active catalyst must contain a vacant $d_{x^2-y^2}$ orbital. Molecular orbital analysis indicates that the LUMOs of **1a**,**b** contain 17.2% and 11.5% $d_{x^2-y^2}$ orbital of the rhodium atom (Figure 2), respectively. Therefore, species **1a**,**b** can accept the π electrons of alkenes. Therefore, **1a**,**b** could serve directly as the active catalysts for the hydroformylation reaction.

2. Catalytic Cycle of Hydroformylation of Phosphinobutene. Four possible mechanisms for the hydroformylation of phosphinobutene (Scheme S3, Supporting Information) were investigated on the basis of the catalytic cycles of the hydroformylation of olefin catalyzed by the monometallic rhodium catalysts proposed by Wilkinson et al.[12−14] and that of the bimetallic rhodium−chromium catalysts proposed by Coutinho et al.[5] The first path is a chelate associative mechanism, in which the phosphinobutene adopts a chelate coordination mode with the rhodium center through the PH_2− and vinyl terminals (A of Scheme S3). The second path is also an associative mechanism, where the phosphinobutene adopts a monodentate coordination mode with the rhodium center via the vinyl terminal (B of Scheme S3). The third path is a monodentate dissociative mechanism, which is popularly accepted for hydroformylation of alkenes catalyzed by the monometallic Rh catalysts (C of Scheme S3). [12−33] The last path is a chelate dissociative mechanism in which the phosphinobutene also adopts a chelate coordination mode with a five-coordinated rhodium center (D of Scheme S3). In the following sections, the four mechanisms are first discussed in detail. Then, a comparison of the four mechanisms is addressed. In light of the regioselectivity of this hydroformylation process, the phosphinobutene addition and insertion steps as well as the branched pathways of each mechanism are discussed in detail. The linear pathways of each mechanism are represented briefly. The *R* pathways are neglected, because the *R* and *S* pathways are

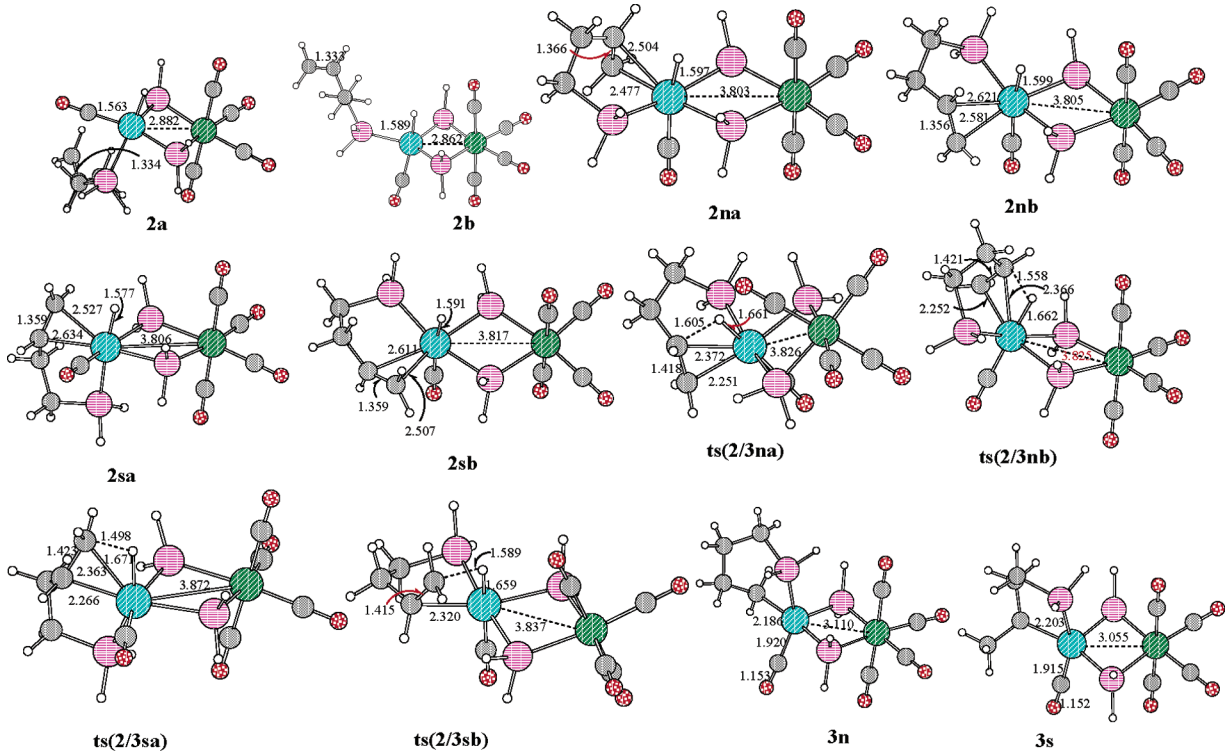

Figure 4. Key structures involved in phosphinobutene addition and insertion steps of the chelate associative mechanism and selected parameters. The bond lengths are given in angstroms.

identical in free energy because of the absence of a chiral center in this Rh−Cr catalyst. All of the relative free energies of the stationary points are referenced to the free energies of **1a** + **re** (phosphinobutene) + CO + H_2 in the gas phase and benzene solution, respectively, in order to immediately compare the relative free energies of the stationary points standing on various pathways of the four mechanisms.

A. Chelate Associative Mechanism. We first discuss the case where the key species adopts chelate coordination with the rhodium center. This mechanism mainly involves the following steps: olefin insertion, carbonyl insertion, H_2 oxidative addition, and aldehyde elimination. In the following sections, these steps are analyzed in detail.

(i) Phosphinobutene Addition and Insertion Steps. The free energy profiles for phosphinobutene addition and insertion in the gas phase and benzene solution are presented in Figure 3. The optimized structures involved in the two steps and selected parameters are depicted in Figure 4. Initially, the PH_2 terminal of the reactant (phosphinobutene) coordinates to species **1a**,**b** to generate the monodentate species **2a**,**b** through ligand exchange. This process is predicted to be exothermic by 6.67 and 20.65 kJ/mol, respectively. Then, the vinyl terminal of phosphinobutene is π-coordinated to the rhodium center to produce the chelate η^2-olefin species **2**. For the chelate η^2-olefin species **2**, only the structures suitable for the subsequent olefin insertion were optimized in the present study. Six isomers for the η^2-olefin species **2** were located. There are two isomers for the chelate η^2-olefin species **2** in *R*- and *S*-branched pathways, respectively. Additionally, there should be other two structures such as **2na**,**nb** with their hydride trans to PH_2, but we failed to locate these two isomers as minima, since the very large twisted force of the five-membered ring makes them unstable (Figures 3 and 4). Because the Rh(I) metal center adopts a 20-electron configuration, there is no strong metal−olefin bonding interaction in the species **2na**,**nb**,**sa**,**sb**, as the bond lengths shown in Figure 4 reflect. Subsequently, the C═C double bond in the phosphinobutene moiety inserts into the Rh−H bond with the formation of the Rh−alkyl species **3** via the transition states **ts(2/3)**. The isomers **2na**,**nb** lead to the formation of the linear species **3n** because the hydride only migrates onto C_β of the phosphinobutene moiety. The free energy barriers of the olefin insertion step are 46.82 and 41.58 kJ/mol for **2na** → **3n** and **2nb** → **3n**, respectively (left side of Figure 3). Simultaneously, the isomers **2sa**,**sb** only result in the branched species **3s**. The free energy barriers for the two pathways of olefin insertion in the branched pathway (the right side of Figure 3) are 61.87 (**2sa** → **3s**) and 51.95 kJ/mol (**2sb** → **3s**), respectively. The energy barriers (58.13 and 50.37 kJ/mol for **ts(2/3sa)** and **ts(2/3sb)**, respectively) are obviously lower than those for the monometallic rhodium catalyst at about 69.4 kJ/mol at the B3LYP/SBK(d) and CCSD//B3LYP levels[28] and about 87.8 kJ/mol at the MP2//RHF level,[26] which indicates that the bimetallic catalyst is more active than the monometallic rhodium catalyst.

As expected, along with olefin insertion, Rh−H, C_α−C_β, and Rh−$C_{\alpha(\beta)}$ are weakened, while Rh−$C_{\beta(\alpha)}$ and $C_{\alpha(\beta)}$−H are strengthened. A comparison of the geometries of the species involved in the olefin insertion step makes it clear that the transition states occur early along the reaction coordinate. Simultaneously, along with the olefin insertion process, the distance between Rh and Cr atoms increases slightly from the chelate η^2-olefin species **2** (about 3.80 Å) to **ts(2/3)** (about 3.85 Å) and then decreases from **ts(2/3)** to **3** (about 3.0 Å). In addition, the conformations of the metallacycle (Rh−C_β−C−C−P) in the chelate η^2-olefin species (**2sa**,**sb**), transition states (**ts(2/3sa)** and **ts(2/3sb)**), and Rh−alkyl species **3s** are in the envelope form (Figure 4). In species **3n**, the metallacycle (Rh−C_α−C_β−C−C−P) adopts a half-boat form (Figure 4).

As shown in Figure 3, the solvation free energy for the species involved in olefin addition and insertion steps is about 10 kJ/mol. Also, the free energies of both activation and reaction in benzene solution are comparable with the data in the gas

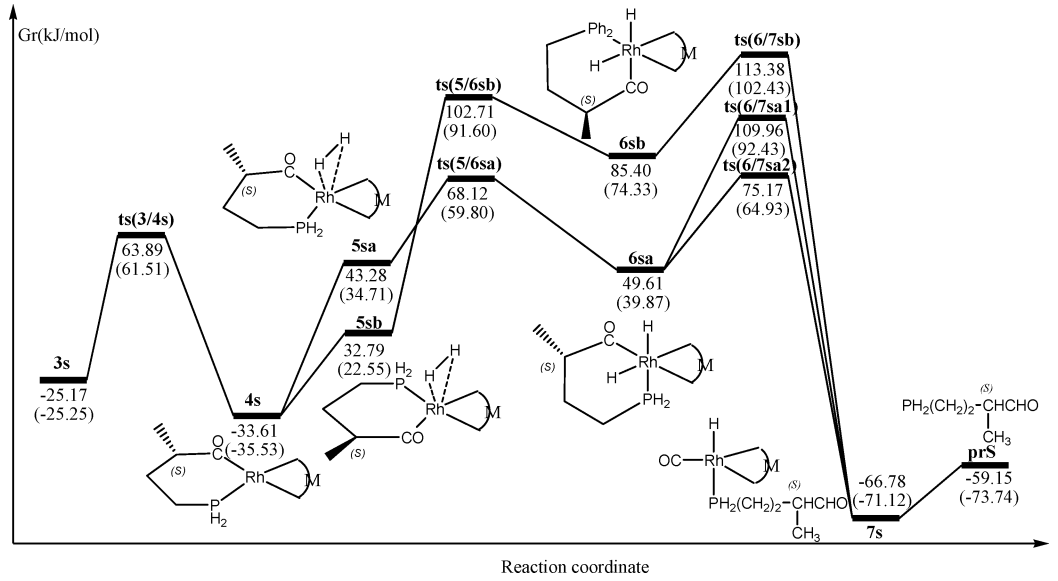

Figure 5. Free energy profile of the CAB path in the gas phase and benzene solution (values in parentheses) at 353.15 K and 27.22 atm.

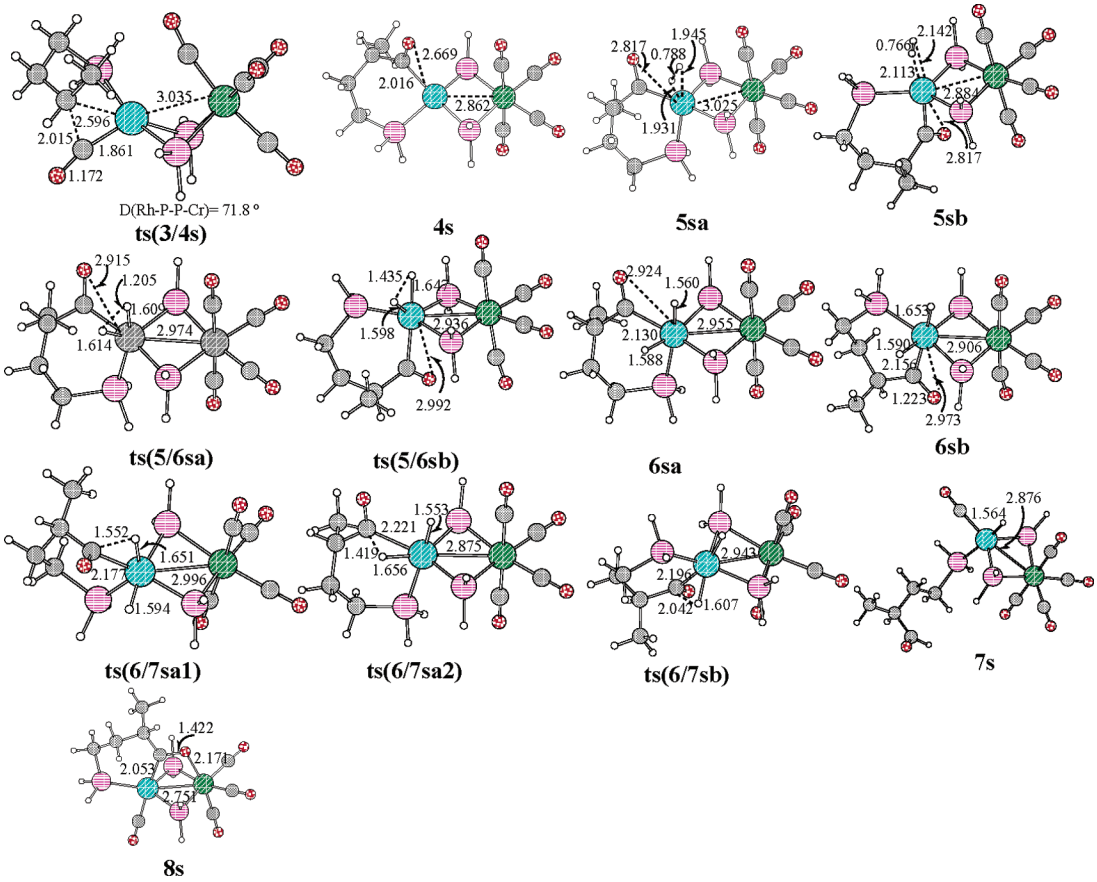

Figure 6. Key structures involved in the CAB path and selected parameters. The bond lengths are given in angstroms.

phase. Therefore, the solvent effect is not significant for the olefin addition and insertion steps.

(ii) Branched Pathways (Path CAB). As shown in Scheme 3, the chelate associative mechanism for the hydroformylation of phosphinobutene starting from species **3** includes the following steps: carbonyl insertion, H_2 oxidative addition, and aldehyde elimination. The calculated free energy profile in the gas phase and benzene solution is shown in Figure 5. The optimized structures and selected parameters are given in Figure 6.

In the first instance, the carbonyl cis to the alkyl in **3s** migrates onto alkyl to form the Rh−acyl species **4s** via the transition state **ts(3/4s)**. The free energy barrier for the carbonyl insertion step is 89.06 kJ/mol in the gas phase and 86.76 kJ/mol in benzene solution. These values are close to those obtained in a number of earlier theoretical studies on monometallic Rh catalyst systems.[15,20,56,57] At the same time, another Rh−acyl species, **8s**, in which the acyl group (Figure 6) coordinated to rhodium was located. Our theoretical studies make it clear that species **4s** and **8s** are in equilibrium and species **4s** is slightly more stable than species **8s**. This result is in line with the experimental study.[5] Simultaneously, the calculated vibrational frequencies of C═O are 1757 cm^{-1} for **4s** and 1584 cm^{-1} for **8s**, which are

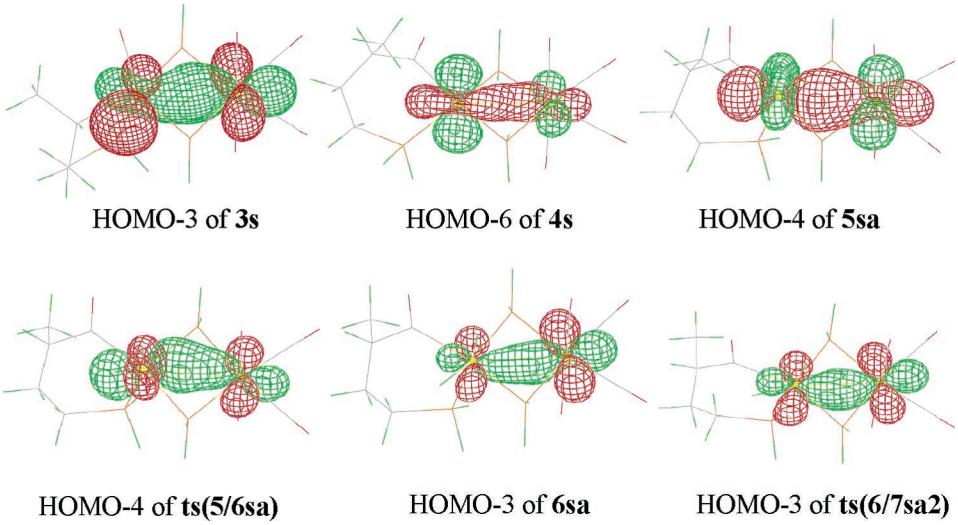

Figure 7. Molecular orbitals containing Rh and Cr orbital interactions of the key intermediates and transition states (cutoff 0.03; only the atomic orbitals of Rh and Cr are depicted).

also in good agreement with the experimental IR data (the experimental ν(C═O) value is 1625 cm^{-1} for **8s**).[5]

Then, the coordination of an H_2 molecule to the rhodium center of **4s** produces the η^2-H_2 adducts **5sa**,**sb** accompanied by H_2 activation. Thereafter, the dihydride species **6sa**,**sb** are formed through the H_2 oxidative addition transition states **ts(5/6sa)** and **ts(5/6sb)**. The H_2 molecule attacks **4s** with H−H bond parallel to linear μ-PH_2−Rh−PH_2R and μ-PH_2−Rh−C(acyl) directions resulting in pathways **4s** → **5sa** → **ts(5/6sa)** → **6sa** and **4s** → **5sb** → **ts(5/6sb)** → **6sb** (Figures 5 and 6), respectively. The free energy barriers for the two pathways are 24.84 (**5sa** → **6sa**) and 69.92 kJ/mol (**5sb** → **6sb**), respectively. The free energy barrier is higher than that of the monometallic rhodium catalyst in the previous theoretical study at the B3LYP/6-31G(d,p)-LANL2DZ(d) level.[58] Therefore, the introduction of the $Cr(CO)_4$ moiety makes the H_2 oxidative addition difficult.

Finally, one hydride cis to acyl in **6sa**,**sb** migrates onto acyl to produce the Rh−aldehyde species **7s**. The two hydride ligands in **6sa** have different chemical environments, and both of them can move onto C(acyl); therefore, there are two transition states (i.e. **ts(6/7sa1)** and **ts(6/7sa2)**) associated with **6sa**. However, there is only one hydride ligand cis to acyl in **6sb**; thus, there is only one transition state connecting **6sb.** The free energy barriers for the three pathways are 52.35, 25.56, and 27.98 kJ/mol (Figure 5), respectively. The free energy barriers for the reverse reactions of the three pathways **6s** → **7s** are obviously much higher (Figure 5). Therefore, the reductive elimination is irreversible and it is in step with the previous theoretical studies[15−33] and the hypotheses based on experimental data.[5,6,12−14]

Figure 5 indicates that the solvation free energies for these species involved in the carbonyl insertion, H_2 oxidative addition, and aldehyde elimination steps are in the range of 0.08−11.00 kJ/mol. Furthermore, the free energies of activation and reaction in benzene solution are comparable with the data in the gas phase. Additionally, all of the metallacycles (Rh−C_{acyl}−C_β−C−C−P) at these stationary points on the free energy profile of the CAB path are in half-chair form.

According to the results obtained from each elementary step, there are a number of possible pathways for the hydroformylation catalytic cycle, originating from **1a**,**b**. The preferred pathway for the CAB path is **1a** → **2a** → **2sa** → **ts(2/3sa)** → **3s** → **ts(3/4s)** → **4s** → **5sa** → **ts(5/6sa)** → **6sa** → **ts(6/7sa2)** → **7s**. The rate-determining step is carbonyl insertion, in both the gas phase and benzene solution. The introduction of the $Cr(CO)_4$ moiety makes the olefin insertion and carbonyl insertion steps easy and the H_2 oxidative addition step difficult.

In Figure 7, the molecular orbitals containing Rh and Cr orbital interactions of the key intermediates and transition states, in which the corresponding antibonding orbital is unoccupied, are shown, while the other related orbitals are shown in Figure S1. The molecular orbitals presented in Figure 7 exhibit the existence of a d orbital interaction between rhodium and chromium atoms throughout the CAB path, except for **ts(3/4s)**. Simultaneously, the calculated Wiberg bond indices of Rh−Cr in **3s**, **ts(3/4s)**, **4s**, **5sa**, **ts(5/6sa)**, **6sa**, and **ts(6/7sa2)** are 0.14, 0.08, 0.18, 0.14, 0.14, 0.13, and 0.21 au, respectively. Therefore, the cooperativity of chromium works through direct orbital interaction in the CAB path.

(iii) Linear Pathways (Path CAL). The CAL path is very similar to the CAB path. The free energy profile of the CAL path in the gas phase and benzene solution is given in Figure 8. The optimized structures and selected parameters are shown in Figure S2 (Supporting Information).

When the structures in Figure S2 are compared with those in Figure 6, it is seen that the species from **3n** to **7n** in the CAL path are structurally similar to **3s**−**7s** in the CAB path, except that the six-center Rh−C−C−C−C−P and seven-center Rh−(C═O)−C−C−C−C−P cycles replace the five-center Rh−(*S*-$CHCH_3$)−C−C−P and six-center Rh−(C═O)−(*S*-$CHCH_3$)−C−C−P cycles. The species on the CAL path are obviously higher in free energy than the corresponding species on the CAB path in the gas phase and benzene solution (Figures 5 and 8). The free energy profile shown in Figure 8 clearly implies that the preferred pathway is **1b** → **2b** → **2nb** → **ts(2/3nb)** → **3n** → **ts(3/4n)** → **4n** → **5na** → **ts(5/6na)** → **6na** → **ts(6/7na2)** → **7n**. The rate-limiting step is also carbonyl insertion with free energy barriers of 81.01 and 107.42 kJ/mol in the gas phase and benzene solution, respectively. The solvent effects on the CAL path are similar to those of the CAB path except for **3n**. The solvation free energy for **3n** is 27.29 kJ/mol, which makes the carbonyl insertion step difficult in benzene solution.

(56) Sakaki, S.; Ikei, M. *J. Am. Chem. Soc.* **1991**, *113*, 5063−5065.
(57) Koga, N.; Morokuma, K. *J. Am. Chem. Soc.* **1993**, *115*, 6883−6892.
(58) Li, M.; Luo, X.; Tang, D. *Acta Chim. Sin.* **2004**, *62*, 1128−1133.

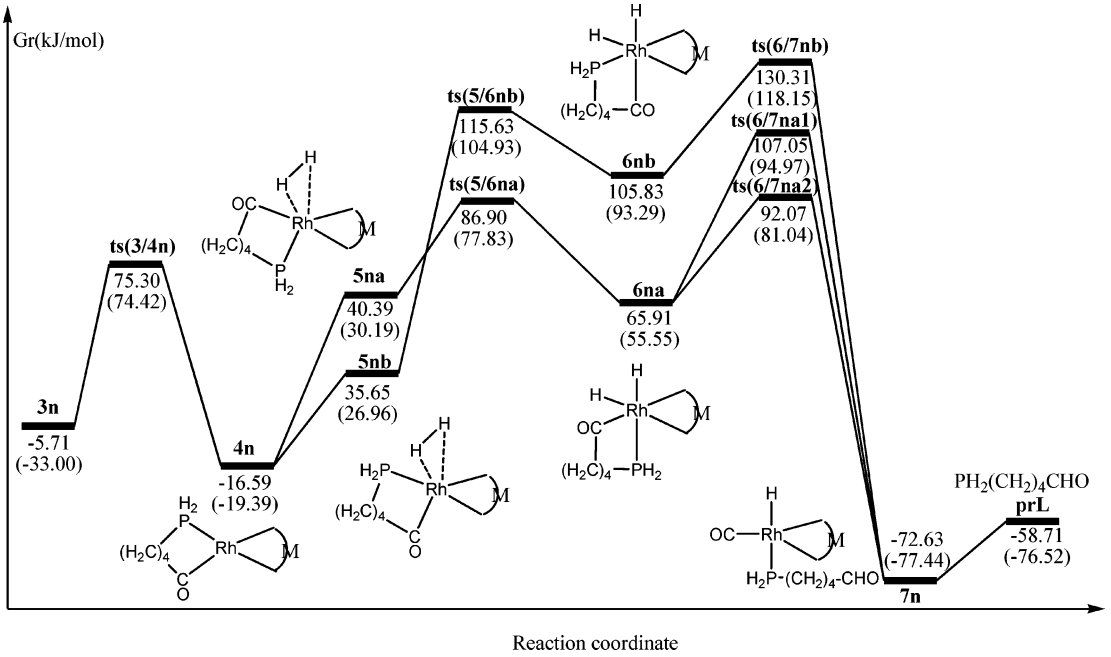

Figure 8. Free energy profile of the CAL path in the gas phase and benzene solution (values in parentheses) at 353.15 K and 27.22 atm.

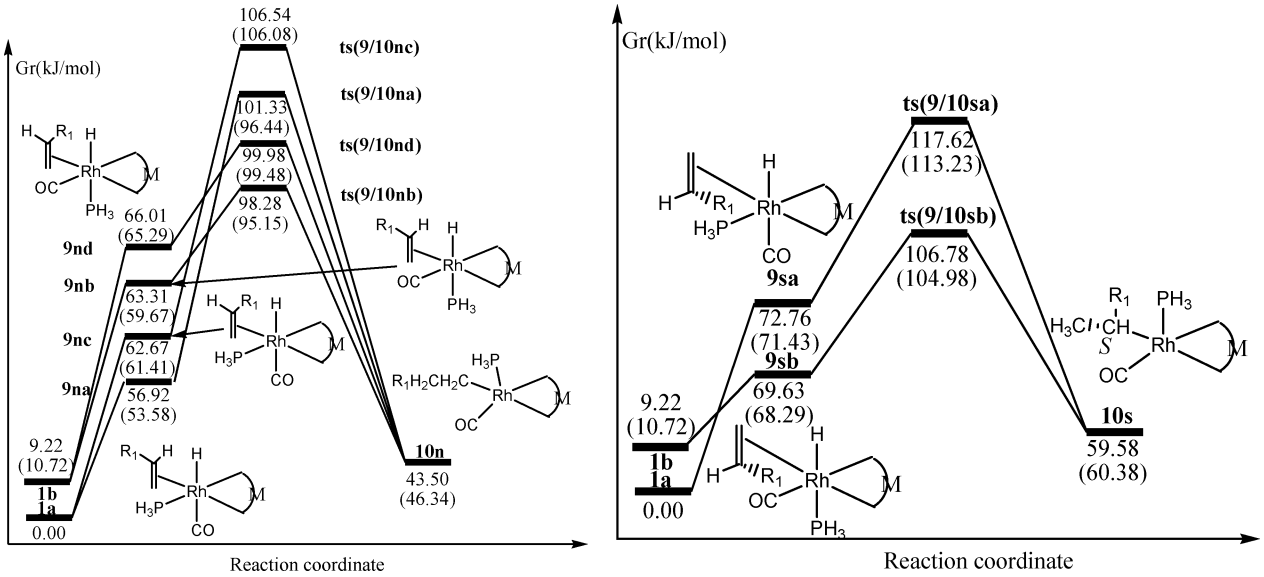

Figure 9. Free energy profiles of olefin addition and insertion steps of the monodentate associative mechanism in the gas phase and benzene solution (values in parentheses) at 353.15 K and 27.22 atm ($R_1 = -CH_2CH_2PH_2$).

B. Monodentate Associative Mechanism. The monodentate associative mechanism is similar to the chelate associative mechanism. The free energy profiles in the gas phase and benzene solution are given in Figures 9−11. The optimized structures and selected parameters are shown in Figure S3 (Supporting Information).

(i) Phosphinobutene Addition and Insertion Steps. The free energy profiles for phosphinobutene addition and insertion steps in the gas phase and benzene solution are presented in Figure 9. The structures involved in the two steps and selected parameters are depicted in Figure S3.

The first step of the monodentate associative mechanism is the coordination of phosphinobutene to the catalysts **1a**,**b** to produce the six-coordinated η^2-olefin species **9**. Eight isomers of species **9** were located. There are two isomers for species **9** in *R*- and *S*-branched pathways, respectively. The two isomers on *R*-branched pathways are neglected. Therefore, only six of them are presented in Figure S3. The six reaction channels are strongly endergonic (Figure 9). The bond length of the C═C double bond in species **9** is slightly longer than that in the free phosphinobutene, which implies that the C═C double bond is activated through olefin addition. The second step in the monodentate associative mechanism is C═C double bond insertion into the Rh−H bond with formation of the Rh−alkyl species **10n**,**s** via the four-center Rh−H−C−C transition states **ts(9/10)**. In this step, the Rh−H bond is cleaved and the vinyl moiety [η^2-(CH_2═CH−)Rh] converts to an alkyl moiety (−CH_2-CH_2−Rh or −$CH(CH_3)$−Rh). The variations of the key bond lengths in these pathways are very similar to those of the chelate associative mechanism (Figure S3). All six pathways are exothermic, as Figure 9 reflects. The free energy barriers of the six pathways are in the range of 33.50−45.00 kJ/mol. The pathways producing the linear species **10n** are more favorable than those producing the branched species **10s**. Obviously, the

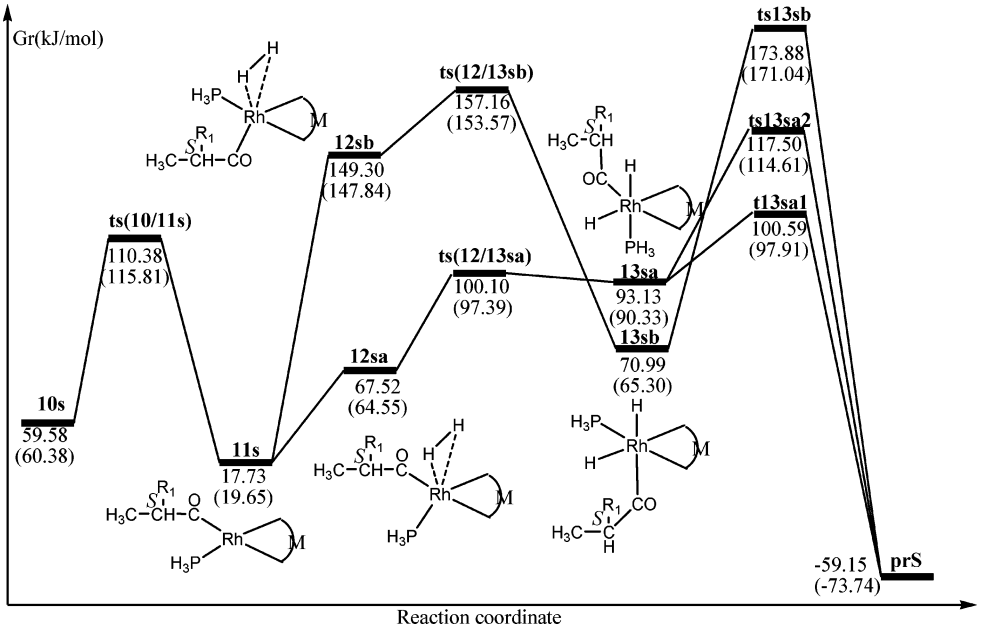

Figure 10. Free energy profile of the MAB path in the gas phase and benzene solution (values in parentheses) at 353.15 K and 27.22 atm ($R_1 = -CH_2CH_2PH_2$).

olefin insertion step of the monodentate associative mechanism is kinetically more feasible than that of the chelate associative mechanism. However, the olefin insertion step of the chelate associative mechanism is thermodynamically more favorable than that of the monodentate associative mechanism, because the relative free energies of all stationary points standing on the monodentate associative mechanism are higher than those of the corresponding stationary points on the chelate associative mechanism. The free energies of solvation for all of the species are about −6.00 to +3.00 kJ/mol in comparison with those of the reactants, but the basic features of the free energy profile shown in Figure 9 remain unchanged.

(ii) Branched Pathways (Path MAB). The alkyl species **10s** obtained from the olefin insertion step can continue the hydroformylation with carbonyl insertion, H_2 oxidation, and aldehyde elimination to render the product **prS**. The calculated free energy profile is depicted in Figure 10. The geometries of all the stationary points obtained in the gas phase are given in Figure S3.

According to Figure 10, first the acyl species **11s** is generated through the carbonyl insertion transition state **ts(10/11s)** with a free energy barrier of 50.80 kJ/mol. Next, the η^2-H_2 complexes **12sa**,**sb** form with the H−H bond parallel to PH_3−Rh−μ-PH_2 and μ-PH_2−Rh−acyl (Figure S3), which is endothermic by 49.79 and 131.57 kJ/mol, respectively. Then, the dihydride species **13sa**,**sb** can be easily formed via the H_2 oxidative addition transition states **ts(12/13sa)** and **ts(12/13sb)**, respectively. Finally, the product **prS** is obtained from the dihydride species **13sa**,**sb** via the aldehyde elimination transition states **ts13sa1**, **ts13sa2**, and **ts13sb** associated with the regeneration of the catalysts **1a**,**b**. The pathway in which the H_2 molecule attacks **11s** with the H−H bond parallel to μ-PH_2−Rh−acyl is quite unlikely kinetically and thermodynamically, with very high relative free energies and free energy barriers. While the profile of the pathway with the H−H bond parallel to PH_3−Rh−μ-PH_2 is relatively smooth, indicative of a preferred reaction manner. The solvent effects on these reaction channels are small (Figure 10). The profile in benzene solution follows the same trend as that in the gas phase.

On the basis of the above discussions, it is seen that the most preferred pathway producing the branched product **prS** in the monodentate associative mechanism is mainly through the following pathway: **10s** → **ts(10/11s)** → **11s** → **12sa** → **ts(12/13sa)** → **13sa** → **ts13sa1**. The rate-limiting step for this pathway is carbonyl insertion, with a free energy barrier of 50.80 and 55.43 kJ/mol in the gas phase and benzene solution, respectively. The relative free energies of the stationary points on these pathways are larger than those standing on the chelate associative mechanism, which implies that the monodentate associative mechanism is not favorable thermodynamically under the experimental conditions.

(iii) Linear Pathways (Path MAL). The formation of the linear product **prL** from the linear alkyl species **10n** via carbonyl insertion, H_2 oxidative addition, and aldehyde elimination constitutes the MAL path. The calculated free energy profile is presented in Figure 11, and the optimized structures involved in the MAL path and selected parameters are given in Figure S3.

The free energy pattern for the MAL path from **10n** to **prL** is similar to that of the MAB path. The carbonyl insertion of **10n** evolving into the acyl species **11n** is exothermic by 33.80 kJ/mol, with a free energy barrier of 42.81 kJ/mol. The acyl species **11n** results in the product **prL** through first a reversible H_2 oxidative addition with the H−H bond parallel to PH_3−Rh−μ-PH_2 and then irreversible aldehyde elimination associated with the regeneration of **1a**,**b**. The two steps in this reaction process have low barriers, indicative of a favorable reaction manner. However, the pathway forming **prL** from **11n** via H−H bond attack on μ-PH_2−Rh−acyl is quite unfavorable, with very high free energy barriers (Figure 11). For these pathways, the solvent effect is small, which is similar to the MAB path discussed above. Therefore, the most favorable pathway for the MAL path is described as **10n** → **ts(10/11n)** → **11n** → **12na** → **ts(12/13na)** → **13na** → **ts13na1**. The rate-limiting step is carbonyl insertion with a free energy barrier of 42.81 and 43.57 kJ/mol in the gas phase and benzene solution, respectively. The relative free energies of the stationary points on the MAL path are higher than those standing on the CAL path, which again indicates that the monodentate associative

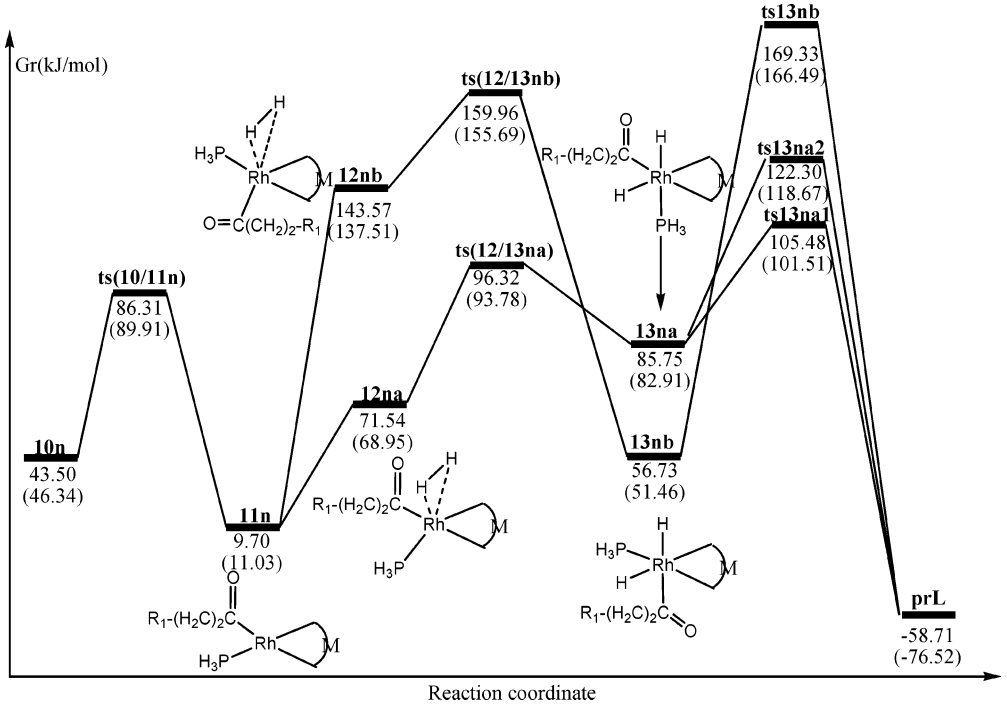

Figure 11. Free energy profile of the MAL path in the gas phase and benzene solution (values in parentheses) at 353.15 K and 27.22 atm ($R_1 = -CH_2CH_2PH_2$).

mechanism is not favorable thermodynamically under the experimental conditions.

C. Monodentate Dissociative Mechanism. The dissociative mechanism of the monometallic rhodium catalyst catalyzed hydroformylation has been well studied in the literature.[15−33] The free energy profiles of the monodentate dissociative mechanism in the gas phase and benzene solution are given in Figures 12−14. The optimized structures and selected parameters are shown in Figure S4 (Supporting Information).

(i) Phosphinobutene Addition and Insertion Steps. The first step of the monodentate dissociative mechanism is the PH_3 ligand dissociation of the catalysts **1a**,**b**, leading to the formation of the active catalyst **1c** with a planar four-coordinated rhodium center. This step is predicted to be slightly exothermic, which means that the catalysts **1a**,**b** would spontaneously lose the PH_3 ligand (Figure 12). Second, the coordination of phosphinobutene to the active catalyst **1c** generates the η^2-alkene species **14a**,**b**, in which the C═C double bond is vertical to the Rh−H bond (Figures 12 and S4). The C═C double bond is obviously more activated in this step than in the above associative mechanisms, as the bond lengths of the C═C double bond suggest (Figures 4, S3, and S4). The differences in the activation are caused by the overlap manner of the $d_{x^2-y^2}$ orbital of rhodium and the π orbital of the vinyl moiety. The phosphinobutene addition is predicted to be endothermic by about 45 kJ/mol, which indicates that the monodentate dissociative mechanism is not favorable thermodynamically. Then, C═C double-bond insertion into the Rh−H bond leads to the formation of the four-coordinated alkyl species **15n**,**s** through **ts(14/15na)**, **ts(14/15nb)**, and **ts(14/15s)** with free energy barriers of 53.77, 33.69, and 38.73 kJ/mol, respectively. The free energy of solvation is relatively small for all species, and the free energy profile obtained in the gas phase is not significantly changed by the bulk solvent effect.

(ii) Branched Pathways (Path MDB). Once the unsaturated alkyl species **15s** is formed, CO can attach to it, resulting in the formation of **16s** under a CO atmosphere, while PH_3, resulting from the generation of the active catalyst **1c**, can attack

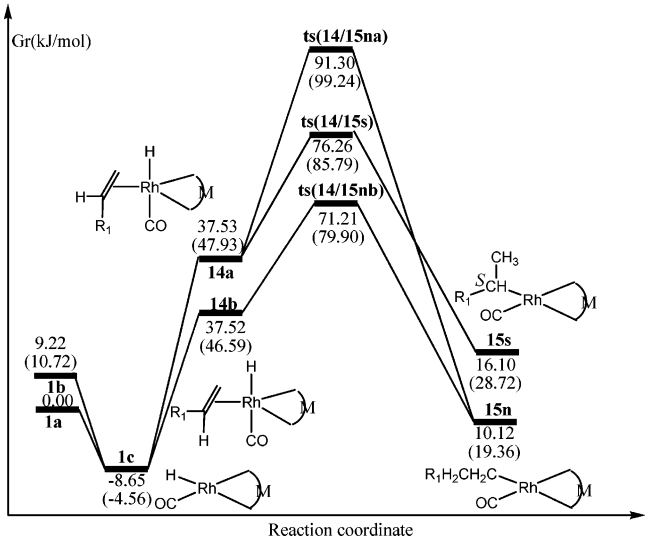

Figure 12. Free energy profile for the alkene addition and insertion steps of the monodentate dissociative mechanism in the gas phase and benzene solution (values in parentheses) at 353.15 K and 27.22 atm ($R_1 = -CH_2CH_2PH_2$).

15s to form **10s**. Then, **16s** and **10s** convert to the product **prS** through carbonyl insertion, H_2 oxidative addition, and aldehyde elimination. Those pathways starting from **10s** have been discussed in the above monodentate associative mechanism. The free energy profile of those pathways originating from **16s** is shown in Figure 13. The corresponding structures and selected parameters are presented in Figure S4.

As reflected by Figure 13, the CO addition is exothermic by 9.16 kJ/mol. This indicates the spontaneity of the CO addition, while the PH_3 coordination is strongly endothermic (Figures 11 and 12). Therefore, the PH_3 coordination is quite unfavorable. When the structures in Figure S4 are compared with those in Figure S3, it is seen that the species from **16s** to **prS** in the MDB path are structurally similar to the species from **10s** to **prS** in the MAB path, except for the replacement of the PH_3

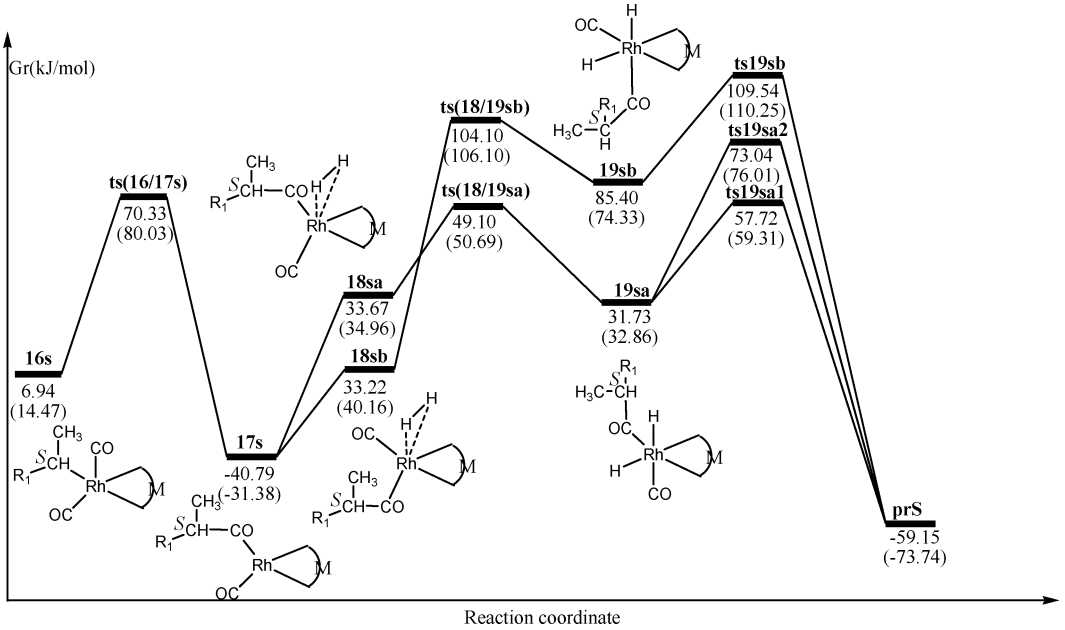

Figure 13. Free energy profile for the MDB path in the gas phase and benzene solution (values in parentheses) at 353.15 K and 27.22 atm ($R_1 = -CH_2CH_2PH_2$).

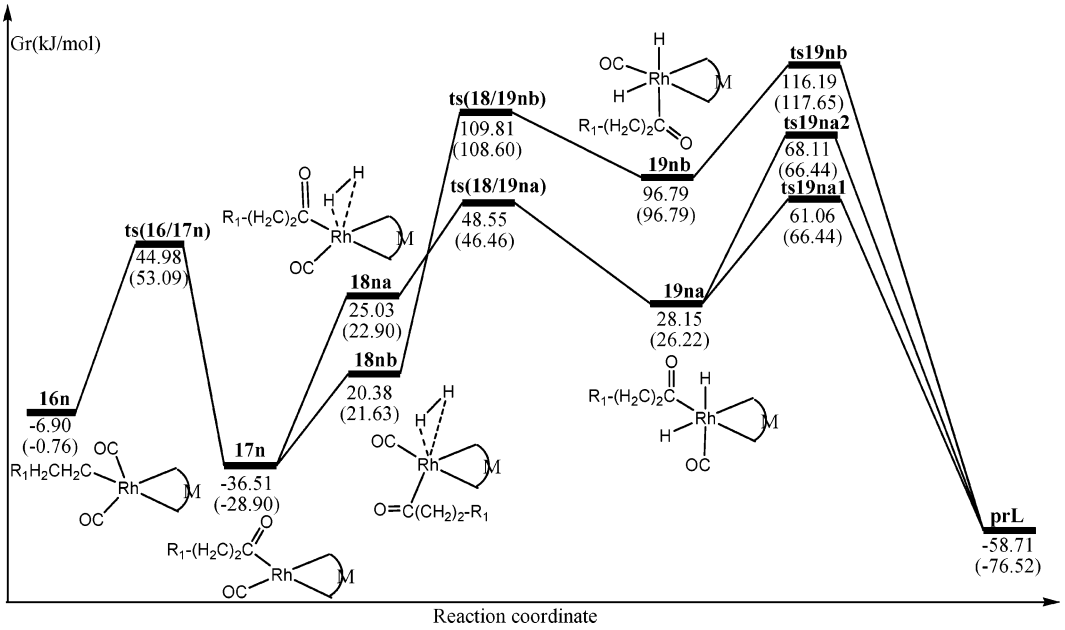

Figure 14. Free energy profile of the MDL path in the gas phase and benzene solution (values in parentheses) at 353.15 K and 27.22 atm ($R_1 = -CH_2CH_2PH_2$).

ligand by the CO ligand. The free energy pattern for the MDB path is very close to that of the CAB path. The carbonyl insertion is exothermic by 47.73 kJ/mol, with a free energy barrier of 63.39 kJ/mol. The conversion of the acyl species **17s** to **prS** is realized through reversible H_2 coordination, reversible H_2 oxidative addition, and irreversible aldehyde elimination. As expected, the attack of the H−H bond on **17s** parallel with CO−Rh−μ-PH_2 is easier than attack parallel with acyl−Rh−μ-PH_2. The solvation free energies relative to that of the reactants on the MDB path are within a span of 12 kJ/mol (from −6.60 to +5.40 kJ/mol). The pattern of the free energy profile in benzene solution is similar to that in the gas phase. The most feasible pathway of the MDB path is **15s → 16s → ts(16/17s) → 17s → 18sa → ts(18/19sa) → 19sa → ts19sa1**, with free energy barriers of 63.39 and 65.56 kJ/mol in the gas phase and benzene solution, respectively.

(iii) Linear Pathways (Path MDL). The free energy profile of the MDL path is shown in Figure 14. The corresponding structures and selected parameters are shown in Figure S4. Similar to the above MDB path, the first step is the attachment of CO or PH_3 to the four-coordinated alkyl species **15n** to form **16n** or **10n** with the similar thermodynamic trends. The corresponding free energy profile shown in Figure 14 is qualitatively similar to that of the MDB path. The free energy barrier of the carbonyl insertion is 51.88 kJ/mol. There are also three reaction channels with the preferred approach of the H−H bond parallel to CO−Rh−μ-PH_2 in the H_2 oxidative addition step. The free energy of solvation of the MDL path is quite similar to that of the MDB path. The most feasible pathway is **15n → 16n → ts(16/17n) → 17n → 18na → ts(18/19na) → 19na → ts19na1**, with carbonyl insertion as the rate-limiting step in both the gas phase and benzene solution.

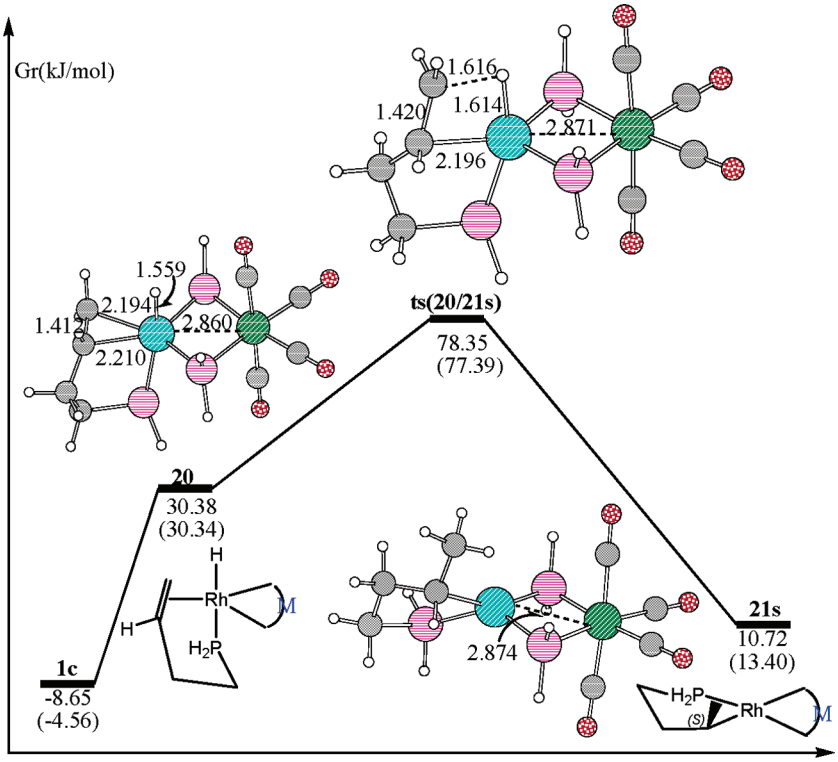

Figure 15. Free energy profile of olefin addition and insertion steps of the chelate dissociative mechanism in the gas phase and benzene solution (values in parentheses) at 353.15 K and 27.22 atm. Bond lengths are in angstroms.

D. Chelate Dissociative Mechanism. The chelate dissociative mechanism is only different from the chelate associative mechanism in the olefin insertion and CO addition steps. There is only one pathway producing the branched product because of the large twisting force of the five-membered ring. The free energy profile of the pathway is presented in Figure 15. The corresponding structures and selected parameters are also shown in Figure 15.

As shown in Figure 15, the formation of the chelate η^2-olefin species **20** is endothermic by 39.03 kJ/mol. The C═C double bond is perpendicular to the Rh−H bond with deep activation of the C═C double bond. Subsequently, the C═C double bond inserts into the Rh−H bond to produce the four-coordinated alkyl species **21s**. It is predicted to be exothermic by 19.66 and 22.94 kJ/mol with a free energy barrier of 47.97 and 47.05 kJ/mol in the gas phase and benzene solution, respectively. Then, a CO molecule attaches to the species **21s** to form species **3s** with an exothermicity of 35.89 kJ/mol. As suggested by Figures 3 and 15, the chelate dissociative mechanism is not favorable thermodynamically and kinetically.

E. Comparison of the Four Mechanisms. To gain a complete understanding of the mechanistic pathways, the free energy profiles obtained with the four mechanisms, shown in Figures 3, 5, 8, and 9−15, must be compared. The first conclusion drawn from this comparison is that the olefin insertion and carbonyl insertion steps of the chelate associative mechanism are quite preferred, because the relative free energies of the stationary points are below those of the other three mechanisms. The chelate associative mechanism is more favorable than the monodentate associative mechanism because of the stabilization of the chelate coordination for the 20-electron olefin species, while the monometallic rhodium catalyst catalyzed hydroformylation of alkenes and alkynes is predicted to proceed through the dissociative mechanism with the 18-electron olefin species reported in previous theoretical and experimental studies.[15−33] Therefore, the introduction of the $Cr(CO)_4$ moiety alters the mechanism of the rhodium-catalyzed hydroformylation of the olefin. A comparison of the free energy barriers of the two steps with that previously reported on the monometallic Rh catalyst systems[28,58] shows that the introduction of the $Cr(CO)_4$ moiety favors of the olefin insertion and carbonyl insertion steps.

The acyl species **4s**,**n** resulting from the preferred pathways of the chelate associative mechanism may directly convert to the products **prS** and **prL** through H_2 oxidative addition and aldehyde elimination steps, while the acyl species **4s/4n** may result in the acyl species **11s/11n** and **17s/17n** through the incorporation of the external PH_3 and CO ligands, respectively. These processes can be considered as equilibrated ligand exchange reactions in eqs 1 and 2. The large endergonic values

$$\underset{\textbf{4n/4s}}{(\text{acyl-PH}_2)\text{Rh}(\mu\text{-PH}_2)_2\text{Cr(CO)}_4} + \text{PH}_3 = \underset{\textbf{11n/11s}}{(\text{PH}_2\text{-acyl})(\text{PH}_3)\text{Rh}(\mu\text{-PH}_2)_2\text{Cr(CO)}_4} \quad (1)$$

$$\Delta_r G = 26.29\ (30.42)/51.34\ (55.18)\ \text{kJ/mol}$$

$$\underset{\textbf{4n/4s}}{(\text{acyl-PH}_2)\text{Rh}(\mu\text{-PH}_2)_2\text{Cr(CO)}_4} + \text{CO} = \underset{\textbf{17n/17s}}{(\text{PH}_2\text{-acyl})(\text{CO})\text{Rh}(\mu\text{-PH}_2)_2\text{Cr(CO)}_4} \quad (2)$$

$$\Delta_r G = -7.18\ (4.15)/\ -19.91(-9.51)\ \text{kJ/mol}$$

of the PH_3 addition and the relatively high relative free energies of the stationary points on these pathways from **11s/11n** to **prS/prL** (Figures 10 and 11) indicate that the presence of phosphine ligands is not in favor of the H_2 oxidative addition, while the exergonic values of the CO addition and the relatively

Scheme 4. Mechanism of Phosphinobutene Hydroformylation Catalyzed by the Rh−Cr Complex on the Basis of Free Energies (kJ/mol) of Activation and Reaction at the B3LYP/631LANp Level in the Gas Phase and Benzene Solution (Values in Parentheses) at 353.15 K and 27.22 atm ($R_1 = -CH_2CH_2PH_2$)[a]

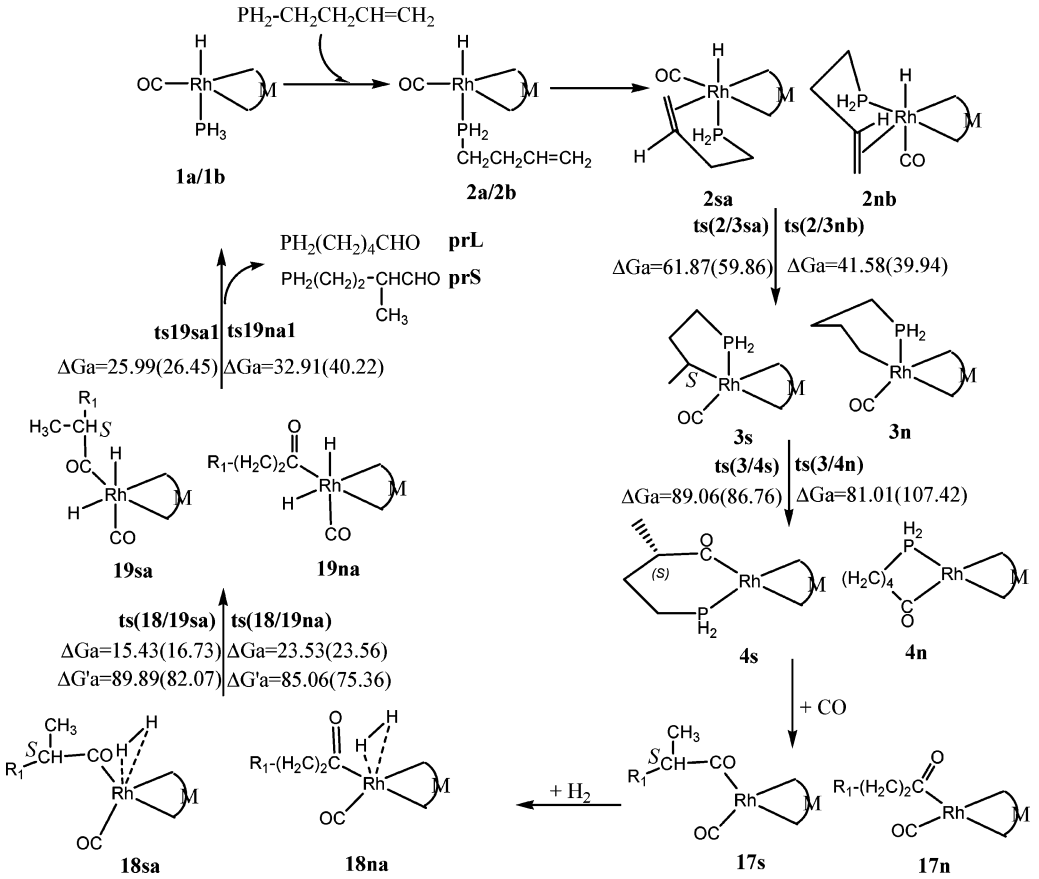

[a] The set of free energy barriers labeled as ΔG_a corresponds to the free energy barrier predicted for the H_2 oxidative addition reaction proceeding from the η^2-H_2 adducts, while those labeled as $\Delta G'_a$ avoid the participation of these adducts in the reaction coordinate.

low relative free energies of the stationary points on these pathways from **17s/17n** to **prS/prL** (Figures 13 and 14) imply that CO concentration or partial pressure is essential for the process of **4s/4n** to **prS/prL**. This is in line with the experimental result that the conversion of the acyl species **4s** and **8s** must involve CO as well as H_2.[5] Therefore, the hydroformylation of phosphinobutene catalyzed by the Rh−Cr bimetallic catalyst involves first the formation of the chelate acyl species (**4n**,**s**) through the chelate associative mechanism including olefin addition, olefin insertion, carbonyl insertion, then CO addition to the chelate acyl species (**4n**,**s**) leading to the formation of the monodentate acyl species (**17n**,**s**), and finally the conversion of the monodentate acyl species (**17n**,**s**) to product aldehyde through H_2 coordination, H_2 oxidative addition, and aldehyde elimination. Carbonyl insertion is the rate-limiting step. This further suggests that the presence of the $Cr(CO)_4$ moiety is able to alter the mechanism of this hydroformylation. Thus, two reaction channels connecting the reactant, phosphinobutene, with the products **prS** and **prL** through **1a** → **2a** → **2sa** → **ts(2/3sa)** → **3s** → **ts(3/4s)** → **4s** → **17s** → **18sa** → **ts(18/19sa)** → **19sa** → **ts19sa1** and **1b** → **2b** → **2nb** → **ts(2/3nb)** → **3n** → **ts(3/4n)** → **4n** → **17n** → **18na** → **ts(18/19na)** → **19na** → **ts19na1** (Scheme 4) are obtained. The rate-limiting step for both reaction channels is carbonyl insertion in the gas phase and benzene solution under the experimental conditions.

3. The Origin of Regioselectivity. From the relative free energies of the reaction channels obtained above in Figure 3, the olefin insertion is reversible and cannot determine the regioselectivity for the present bimetallic system. This is different from previous theoretical studies on the monometallic Rh-catalyzed regioselective hydroformylation predicting the olefin insertion to be irreversible and determinative for the regioselectivity.[16−18] The highest free energy transition state of the branched pathway is lower than that of the linear pathway in the gas phase and benzene solution, as Figures 3, 5, 8, 13, and 14 suggest. Therefore, the branched product is quite favorable thermodynamically. From the free energy barriers of the two reaction channels obtained in Scheme 4, the difference between the branched and linear pathways is so small that the regioselectivity is not obvious (89.06 and 81.01 kJ/mol for branched and linear reaction channels, respectively; Scheme 4). However, the free energy barrier of the carbonyl insertion of **3s** → **4s** is obviously lower than that of **3n** → **4n** in benzene solution (86.76 kJ/mol for **3s** → **4s** and 107.42 kJ/mol for **3n** → **4n**; Scheme 4). Therefore, the regioselectivity of heterobimetallic Rh−Cr-catalyzed hydroformylation is a kinetically controlled process in benzene solution. The free energy differences in benzene solution favor the formation of the branched product with a percentage ratio of nearly 100% both kinetically and thermodynamically under the experimental conditions. This is in good agreement with the experimental data.[4−6] When the molecular orbitals of **ts(3/4s)** and **ts(3/4n),** shown in Figure S1, are compared, it is found that the d orbital interaction between Rh and Cr in **ts(3/4n)** is stronger than that in **ts(3/4s)**. Therefore, the regioselectivity should be attributed to the d orbital interaction between Rh and Cr. The Wiberg bond indices of Rh−Cr also support this point (0.08 au for **ts(3/4s)** and 0.17 au for **ts(3/4n)**). Very interestingly, the Rh−μ-P1−μ-P2−Cr cycle

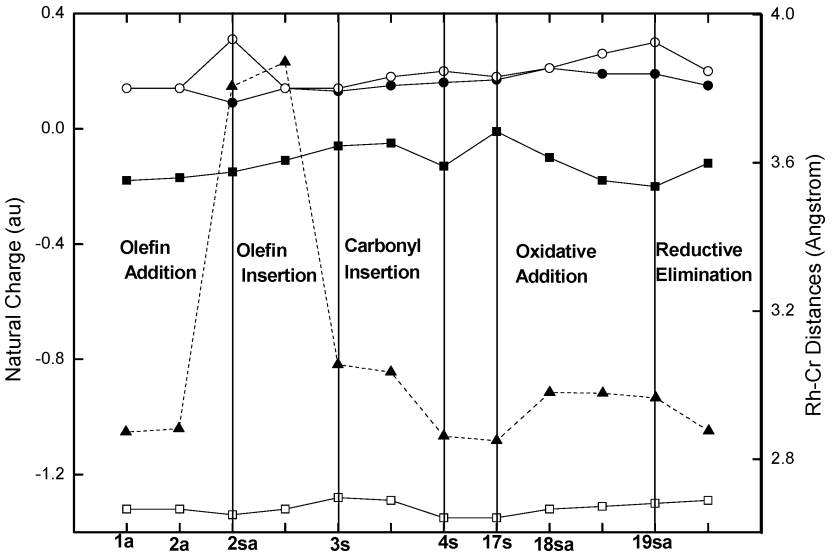

Figure 16. Natural charges of Rh (■), Cr (□), μ-P1 (●), and μ-P2 (○) and Rh−Cr distances (▲) for the preferred pathway of Rh(I)-Cr-catalyzed hydroformylation.

adopts a butterfly form with the dihedral angle Rh−μ-P1−μ-P2−Cr of **ts(3/4s)** of 71.8°, while the dihedral angle Rh−μ-P1−μ-P2−Cr of **ts(3/4n)** is 135.5°.

4. Cooperativity of Chromium. To investigate the cooperativity of chromium, the NPA charges of Rh, Cr, μ-P1, and μ-P2 along with the preferred pathway are depicted in Figure 16. Figure 16 also presents the plot of the Rh−Cr distance along the reaction coordinate. The variation of the Rh−Cr distances in the olefin addition step indicates the breakage of the orbital interaction between Rh and Cr atoms. The breakage of the orbital interactions between Rh and Cr atoms in the olefin addition step can be viewed as the disconnection of the $Cr(CO)_4$ moiety with the catalytic center ($HRh(CO)(PH_3)$ moiety), releasing a vacant $d_{x^2-y^2}$ orbital to accept the π electrons of the alkenes, whereas the two moieties are still connected by the two μ-PH_2 ligands. The orbital interaction between Rh and Cr atoms can re-form in the subsequent steps of the catalytic cycle (Figure 7). Therefore, the olefin addition should correspond to the ligand dissociation and olefin addition steps of the monometallic Rh-catalyzed hydroformylation; that is to say, the ligand dissociation and olefin addition steps of the bimetallic Rh(I)−Cr-catalyzed hydroformylation happen concurrently. Thus, the heterobinuclear Rh(I)−Cr-catalyzed hydroformylation of phosphinobutene proceeds through both associative and dissociative mechanisms. At the same time, this study also demonstrates that the catalysts **1a**,**b** could serve directly as the active catalysts for the hydroformylation reaction. The reformation of the orbital interaction can stabilize the unsaturated alkyl species **3s**. The evolution of the orbital interaction between Rh and Cr atoms in the olefin addition and insertion steps demonstrates that the $Cr(CO)_4$ moiety serves as an orbital reservoir of the catalytic center Rh atom.

In the carbonyl insertion step of **3s** to **4s**, the charges on Rh and Cr atoms increase first from **3s** to **ts(3/4s)** and then decrease in **ts(3/4s)** → **4s**. As shown in Figure 16, the distance between Rh and Cr atoms in the branched pathway is longer than that in the linear pathway for the transition state of the carbonyl insertion step, which demonstrates that the cooperativity of chromium affects the regioselectivity greatly.

The variations of the charges on Rh and Cr atoms in the H_2 oxidative addition and aldehyde elimination steps are smooth. The distances of Rh−Cr shown in Figures S3 and 16 clearly indicate that the orbital interaction between Rh and Cr atoms exists throughout the H_2 oxidative addition and aldehyde elimination steps.

An examination of the natural populations for the Rh, Cr, and two μ-P atoms (Figure 16) reveals an interesting complementary change for the two μ-P atoms. As all the catalytic events occur on the Rh atom, the charge on the Rh atom increases in the olefin addition and insertion steps, while it decreases in the carbonyl insertion and H_2 oxidative addition steps and then increases in the aldehyde reductive elimination step.

Summary and Conclusion

A theoretical study was carried out at the B3LYP level of theory for the $(CO)_4Cr(\mu\text{-}PH_2)_2RhH(CO)(PH_3)$-catalyzed hydroformylation of phosphinobutene. Four mechanisms are possible. The first path is a chelate associative mechanism, in which the main species adopts a chelate coordination mode with the rhodium center. The second path is also an associative mechanism, in which the key species adopts a monodentate coordination mode with the rhodium center. The third path is a monodentate dissociative mechanism, which is similar to the popularly accepted mechanism of hydroformylation of alkenes catalyzed by the monometallic Rh catalysts. The last path is a chelate dissociative mechanism in which the main species also follow a chelate coordination mode. The comparison of the four possible mechanisms indicates that the hydroformylation of phosphinobutene catalyzed by the Rh−Cr bimetallic catalyst is obviously different from the previously characterized mechanism of the monometallic rhodium catalyst. The hydroformylation of phosphinobutene catalyzed by the Rh−Cr bimetallic catalyst involves first the formation of the chelate acyl species (**4n**,**s**) through the chelate associative mechanism, including olefin addition, olefin insertion, and carbonyl insertion steps, then CO addition to the chelate acyl species leading to the formation of the monodentate acyl species (**17n**,**s**), and finally the conversion of the monodentate acyl species to the product aldehyde through H_2 coordination, H_2 oxidative addition, and aldehyde elimination (Scheme 4). Carbonyl insertion is the rate-limiting step for the whole catalytic cycle. Therefore, the introduction of cooperative metallic chromium remodels the mechanism. Also, some other new points have been clarified. (1) The CO concentration or partial pressure is helpful for the

transformation of the chelate acyl species to the product aldehyde. (2) The bimetallic Rh−Cr-catalyzed hydroformylation favors the branched product, with a percentage ratio of nearly 100% both kinetically and thermodynamically in benzene solution. (3) The breakage of the orbital interaction between Rh and Cr atoms in the olefin addition step indicates that this associative mechanism can be viewed as both associative and dissociative. The chromium serves as an orbital reservoir in olefin addition and insertion steps via the variation of the orbital interaction between Rh and Cr atoms. (4) The calculated free energy barriers imply that the catalytic activity of the Rh(I)−Cr bimetallic complex is higher than that of the monometallic Rh catalysts. (5) Theadaptivity of the Rh−μ-P−Cr−μ-P four-membered ring in the reaction process effectively demonstrates the cooperativity of chromium with the catalytic center rhodium. These results are in good agreement with the experimental studies.

Acknowledgment. Financial support from the Teaching and Research Award Program for Outstanding Young Teachers in Higher Education Institutions of the MOE, People's Republic of China, is sincerely acknowledged. We are grateful to the reviewers for their pertinent comments and good suggestions concerning our original paper.

Supporting Information Available: Schemes S1−3, Figures S1−4, the complete ref 34, Tables S1−3 with free energies in the gas phase, the solvation free energies (ΔG^{sol}), and Cartesian coordinates of optimized structures. This material is available free of charge via the Internet at http://pubs.acs.org.

OM0601605